The setting-up of an experiment to study charmonium states at CERN's Intersecting Storage Rings

Bjarne Stugu

Thesis submitted to the degree Cand.Scient
at the University of Oslo, Institute of Physics.

Contents:

discovered independently the existence of a new narrow state at about 3.1 GeV. The width of this state is at least 1000 times smaller than other states in the same mass range. The new state, called J or ψ, was soon interpreted as a bound $q\bar{q}$ system of a new quark type, called charm, and of its antiquark.[5,6]

1.2 The Charmonium Spectroscopy, Experimental Situation

After the discovery of the $\psi(3097)$, a whole new series of states were found, all supposed to be bound states of charm - anticharm quark pairs. In analogy with positronium (e^+e^- bound states) they were called charmonium states. Most experimental work on charmonium so far has been done at e^+e^- colliders at SLAC and DESY. The crystal ball detector at SLAC is ideal for studying charmonium because of its high resolution electromagnetic calorimeter consisting of NaI crystals covering 93% of the full solid angle. Two methods has been used to produce and detect the various $c\bar{c}$ states:

a) To produce them directly in the e^+e^- collisions by adjusting the collision energy to the $c\bar{c}$-resonance rest masses. In this case, the $c\bar{c}$ is produced through a virtual photon, and the $c\bar{c}$ state must have the same quantum numbers as the photon i.e. $J^{PC}=1^{--}$ The process is described diagrammatically in fig. 1.

The $\psi(3097)$, $\psi'(3686)$ and the $\psi''(3770)$ are produced in this way, and have therefore $J^{PC}=1^{--}$.

b) If the state one looks for is not directly accessible in e^+e^- collisions, another, more massive charmonium state must be produced first. The state one wishes to study can then be formed through the

Fig. 4 gives the level diagram and possible radiative transitions between charmonium states below charm threshold. Note that the $^1P_1$ state is not yet found. It is very difficult to find this state in e^+e^- collisions, because it cannot be produced directly due to parity conservation, and the ψ' does not decay into $\gamma\,^1P_1$ because of charge conjugation conservation.

Hence it has to be observed in the cascade process:

$$
\begin{aligned}
e^+e^- \to \psi' & \\
&\hookrightarrow \gamma\eta_c' \\
&\qquad\hookrightarrow \gamma\,^1P_1
\end{aligned}
$$

In table 1 the various states are listed with their properties. The total angular momenta of the χ states are determined from the radiative decay angular distributions The ordering of the masses of the χ states is consistent with what is qualitatively expected. The 2^{++} state has more mass than the 1^{++} and the 0^{++} states etc.

1.3 QCD and Potential Models

Even though the existence of a charmed quark was first predicted in order to explain problems with weak interactions; very important contributions to strong interaction physics has come from the study of charmonium states.

That the mesons and baryons are composed of quarks has become pretty clear the past few years. However, a free quark has never been seen. This has led to the development of a new theory of the strong interactions called Quantum Chromo Dynamics (QCD) where confinement of the quarks inside mesons and baryons is introduced in an axiomatic way.

In QCD one assumes that the quarks have an intrinsic quantum number called color. The quarks can have three different colors; and they transform in color space like the triplet in the fundamental $SU(3)_c$ represetation. A meson consists of a quark and an antiquark while a baryon consists of three quarks. Other bound systems of quarks have not been seen. Moreover only colorless combinations of quarks, color-singlets, exist in nature. As a consequence, quarks can never appear free, they will always be bound, confined in a potential.

Combinations of colored quarks can be done to form new representations of $SU(3)_c$. For example, a quark and an antiquark can combine to form a nine dimensional representation of $SU(3)_c$; meaning basically that three colors can combine with three anticolors in nine different ways. Moreover it can be shown that this representation can be broken down to an invariant one dimensional representation (a singlet), plus an invariant eight dimensional representation (an octet). Formally this is written like this:

$$3 \otimes \bar{3} = 1 \oplus 8$$

The possible $q\bar{q}$ combinations in color space can, if one denotes the three colors by r, b and w, and the three anticolors by $\bar{r}$, $\bar{b}$ and $\bar{w}$, conveniently be expressed as the direct product:

$$\begin{pmatrix} r \\ b \\ w \end{pmatrix} (\bar{r},\bar{b},\bar{w}) = \begin{pmatrix} r\bar{r} & r\bar{b} & r\bar{w} \\ b\bar{r} & b\bar{b} & b\bar{w} \\ w\bar{r} & w\bar{b} & w\bar{w} \end{pmatrix} = M$$

It can be shown that the normalized trace of M

i) asymtotic freedom; i.e. interactions must be weak at short distances.

ii) confinement of the quarks, meaning that the potential must tend to infinity as the quark separation tends to infinity.

The first potential used in the description of the charmonium states is given by:[8]

$$1.2.1 \qquad V(r) = \frac{-k}{r} + ar$$

where the first term accounts for the short range one gluon exchange interaction, while the second term implies confinement, and is based on the assumption that the force between the c and the $\bar{c}$ is constant, independent of r.

Other potentials include a harmonic oscillator potential perturbed with a Coulombic potential [7] .

$$1.2.2 \qquad V = -\frac{k}{r} + \frac{1}{2}\mu\cdot\Omega^2 r^2$$

This potential makes calculations easy, because the harmonic oscillator potential gives exact solutions to the Schrödinger equation.

Another potential which seems to work well is:[9]

$$1.2.3 \qquad V = A+Br^{\alpha}$$

where $\alpha = 0.100$, $A=8.064$, $B=6.870$

The $^1P_1$ state can be seen through the radiative decay of the η'_c. If we can find the resonant mass, it should also be possible to produce it directly.

The partial cross-section for charmonium produced in $p\bar{p}$ collisions and decaying into electromagnetic final states is estimated to be from about 1 to 100 nb at resonant energies [11]. Hadronic final states of $c\bar{c}$ decays will be hard to see due to large background production. (The total $p\bar{p}$ cross-section is about 70 mb at our energies.) Thus, it is necessary to measure electromagnetic final states. Final electromagnetic states from η_c and χ decays must involve photons. Photons are detected using calorimetric methods, but track reconstruction is difficult unless one has a severe constraint on the position of the decay vertex.

Using an antiproton beam circulating in CERN's ISR, with a hydrogen gas jet target, we should obtain a good vertex definition and a good luminosity. With an expected luminosity of nearly 10^{31} $cm^{-2}s^{-1}$, the detection rate of charmonium states should be about 5-50 per hour (depending on the state we are looking for).

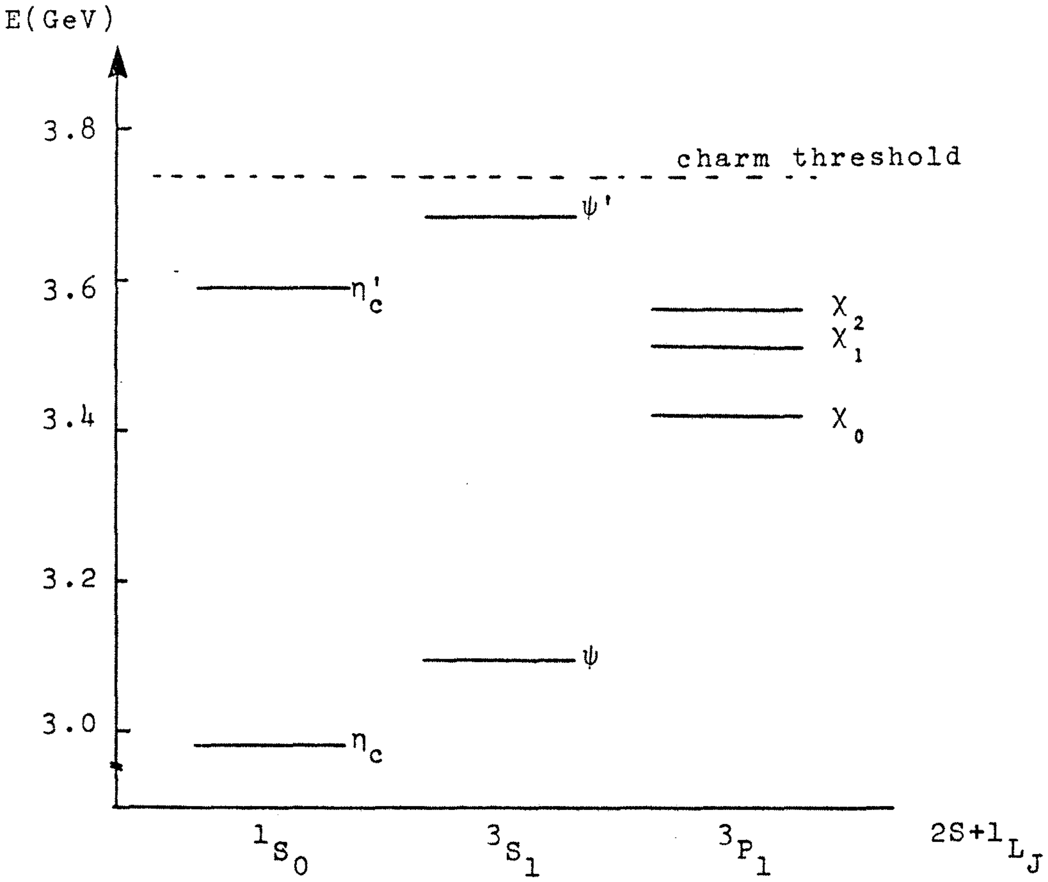

Fig. 1.4 Level diagram of charmonium states below charm threshold.

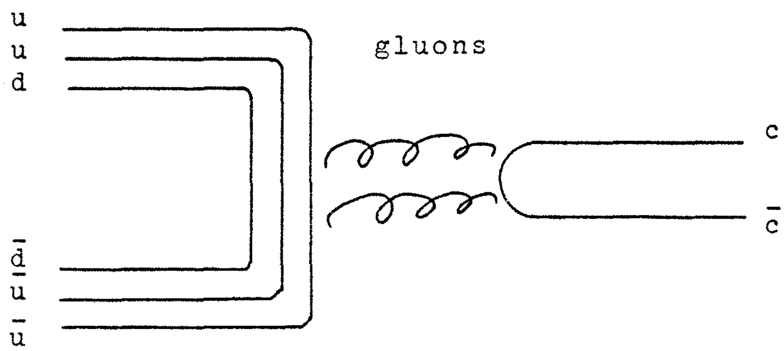

Fig. 1.5 Production of charmonium in p-$\bar{p}$ collisions.

to the normal ISR momenta which are in the range 26 GeV/c -31 GeV/c, and modifications of the acceleration system and routines are therefore necessary. The antiproton energies are below the ISR transition energy, meaning that the phase of the Radio Frequency (RF) acceleration system must be changed. At normal ISR runs, the particles are always injected at energies above the ISR transition energy. The velocity of 3.5 GeV/c protons is significantly below the speed of light, $\beta = \frac{v}{c} \approx 0.96$, so during acceleration, the revolution frequency of the particles is increasing much faster than during acceleration of 26 GeV/c protons.

The intensity of the antiproton beam is limited by the number of particles accumulated in the AA, and by the transfer efficiency of the particles from the AA to the ISR. 2.4×10^{11} antiprotons have been accumulated in the AA, and the transfer efficiency was about 2/3. This gave about 1.5×10^{11} antiprotons in the ISR. The AA performance is however still improving.

The momentum cooling system should be able to keep the momentum spread below $\frac{\Delta p}{p} = 1.5\times10^{-3}$ even when the jet target is operating causing perturbations to the circulating antiproton beam. The momentum spread is equivalent to a horizontal spread in particle orbits. $\frac{\Delta p}{p} = 1.5\times10^{-3}$ corresponds to a width of the beam of about 6 mm. If one is able to determine an interaction vertex to better than 6 mm in the horizontal direction, thia does however not imply a significant improvement in the momentum determination. The reason is that the horizontal oscillations of a particles' path around its equilibrum orbit is of the same magnitude as the spread around the mean orbit. Tests show that the mean

Ref. [13] gives the following formula for the jet speed, when the jet consists of hydrogen molecules.

$$2.2.2 \qquad \omega = \sqrt{\frac{7}{2}}\, \langle v \rangle = 1490 \text{ ms}^{-1}$$

It would be desireable to have liquid hydrogen passing through the ISR tube, because this would give optimal density of the target. It is indeed possible to obtain a condensation of the hydrogen as it expands in the nozzle. The gas expansion is adiabatic, and proceeds along an isentrope which crosses the phase change line in a P-T diagram. After supersaturation the gas condenses into clusters. See fig. 2.3. The nozzle shape is most important for the clustering, and for the angular spread in the cluster beam. Fig. 2.4 reproduces qualitatively results from cluster beam intensity measurements done with different nozzles at CERN [14]. A converging diverging trumpet shaped nozzle turns out to give the best results. (fig.2.4).

The jet is tested to give about 10^{-10} gcm^{-2} over a 6 mm vertical aperture. Then, if we have 2×10^{11} stored antiprotons circulating, the luminosity will be $\approx 0.4 \times 10^{31}$ cm^{-2}s^{-1} which is in reasonable agreement with what was hoped to be reached, (10^{31} cm^{-2}s^{-1}).

2.3 Detectors

We will detect final states involving several γ-particles and/or electron positron pairs. The detectors are arranged in two arms with left-right symmetry with respect to the beam as shown in fig. 2.5. The geometrical acceptance for e^+e^- and $\gamma\gamma$ final states is 13% of the solid angle. Threshold Cerenkov counters are used to identify electrons. Multiwire proportional chambers (MWPC s) are used for charged track reconstruction. The photons

b) <u>The Multiwire Proportional Chambers (MWPCs)</u>

A multiwire proportional chamber consists of several planes of anode wires at ground potential interleaved with cathode planes at a negative potential of several kV. A wire plane consists of parallel wires with a spacing of typically 2 mm. The wires in two planes make an angle with respect to each other. The chambers are filled with a gas which is ionized when a charged particle crosses a chamber. The liberated electrons will then move in the strong electric field towards the nearest anode wires. As the electrons approach a thin anode wire(of diameter typically 20 μm) the electric field increases, and in the vicinity of the wire, the field is so strong that the energy of the free electrons will be large enough to create an avalanche of ions. The main part of the pulse on the anode wire is induced by the heavy positive ions moving slowly away from the wire. Since there are at least two planes of wires in a chamber, the coordinates of the detected particle can be determined to an accuracy equal to about ½ the wire spacing. The MWPCs in our experiment are used in the digital mode, i.e. the pulse from a wire has to pass a certain threshold to be accepted as a signal, and no pulse-height measurements are done.

We have two sets of MWPCs in our experiment for the determination of charged tracks. Each chamber consists of three wireplanes, the X, Y and U planes. The X and Y planes have the wires at right angles to each other while the U plane has its wires at an angle of about 28° to the y plane wires. See fig. 2.6. The U-plane is used to resolve ambiguities from points reconstructed using only the X and Y planes. One of the MWPCs is right in front of the Cerenkov counter, (chamber 1) while the other is right behind it (chamber 2).

scintillator bars, each of width 85.7mm. The gammas which have converted into a charged shower in the precalorimeter, will trigger these counters.

2.4 Veto Counters

The large crossection for $p\bar{p}$ collisions will automatically give background problems. To reduce false triggers caused by high multiplicity events, veto counters are placed outside the acceptance of the detector arms, covering most of the rest of the solid angle. Two types of veto counters are used in order to be able to distinguish charged particles and photons even outside the detector acceptance. The veto counters which detect charged particles are just scintillator plates with a PM readout. Just behind these we find a set of segmented lead-scintillator sandwich detectors capable of detecting photons with some position determination. The thickness of these counters is 4.2 radiation lengths.

Apart from rejecting events, the vetoes will be used to detect photons in $e^+e^-\gamma$ final states. The vetoes will be used to find the multiplicity of the final state, and if the number of photons is too high the event will be rejected at the trigger level.

2.5 The Trigger

At the time of writing, the trigger conditions are being implemented. We will briefly describe how the main features are envisaged.

In any of the final states we are looking for, signals must be present in the two shower hodoscopes, SH1 and SH2. A 14x14 matrix of coincidences is constructed between the 14 counters in SH1 and the instead of in anticoincidence.The allowed multiplicity of a final state is set in the "Majority Decision Unit", the MDU. This unit has been constructed at LAPP (Laboratoire d'Annecy le Vieux de Physique des Particules). The MDU will be programmed to accept events with a multiplicity in the vetoes below a preset number.

Also a microprocessor will be used to reduce the trigger-rate. This processor will read the ADCs of the calorimeters and reject events where the total energy deposited is less than a certain threshold. This takes less time than the read-out time of all Camac units by the data aquisiton computer. Hence the dead time will be reduced.

Monte-Carlo studies have been done on the background reactions. According to these results, the number of events written to tape should be about 35 per second [15].

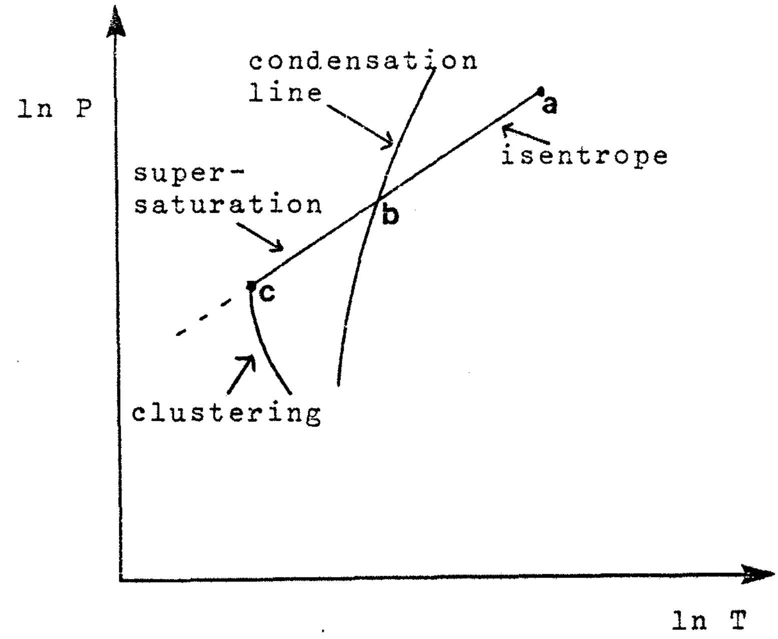

Fig. 2.3 Expansion of a gas in the P-T diagram along an isentrope. The figure is taken from ref. (13)

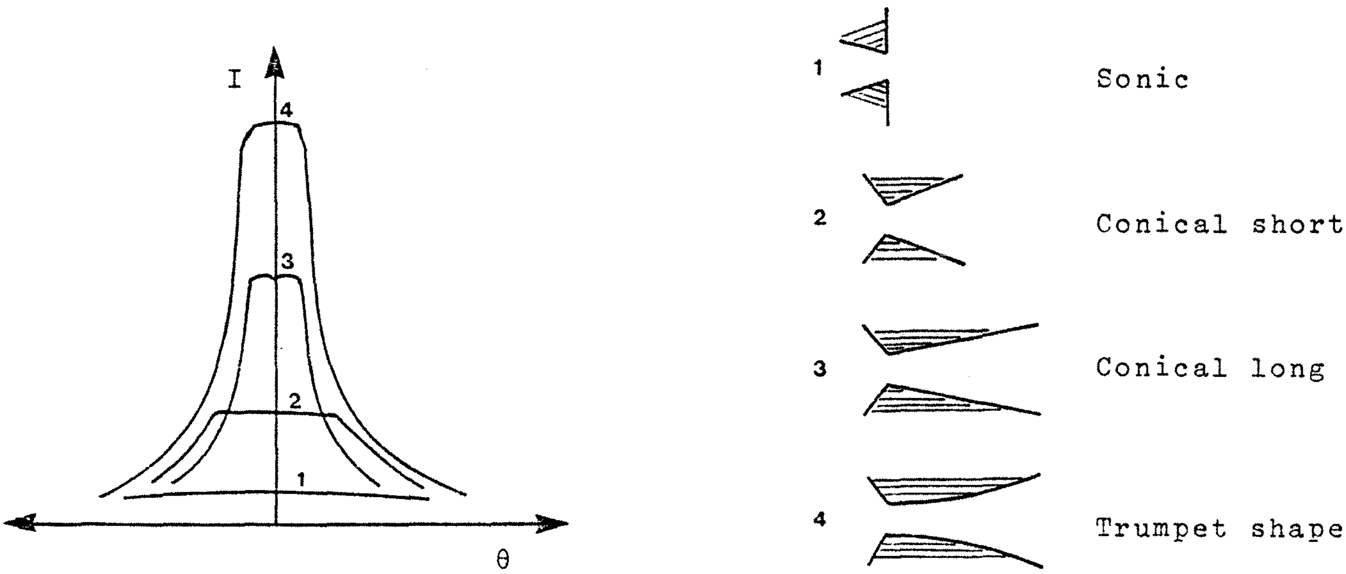

Fig. 2.4 Hydrogen gas intensity distributions for different nozzle shapes.

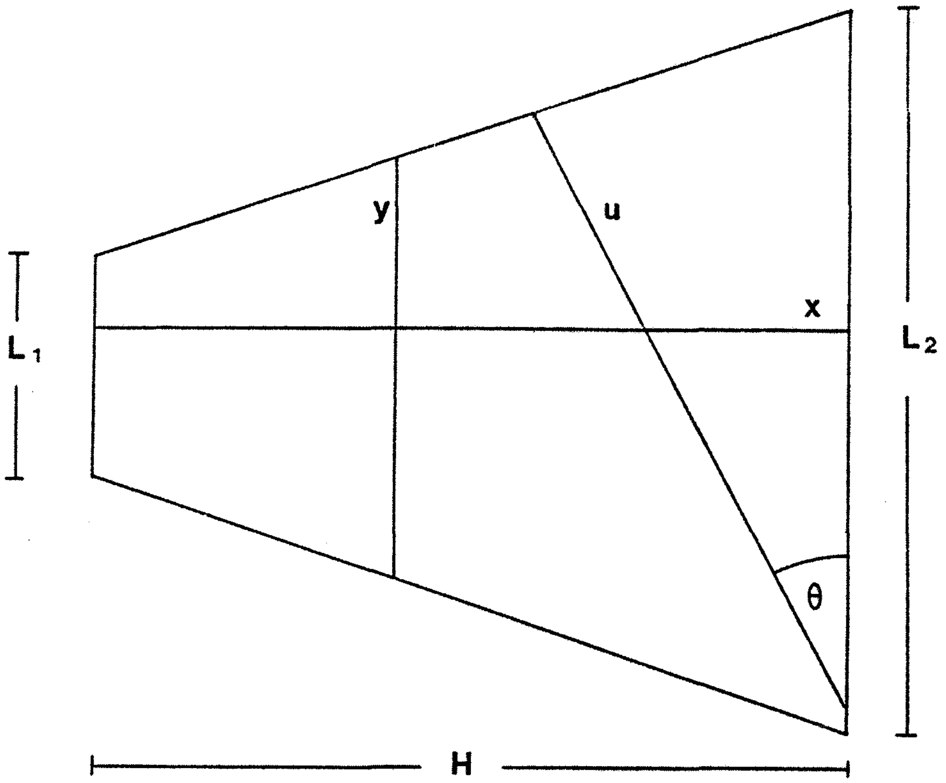

Fig. 2.6 Relative orientation of the wires in the three MWPC planes. θ=28 degrees. The dimensions of the chambers are given in table 2.2.

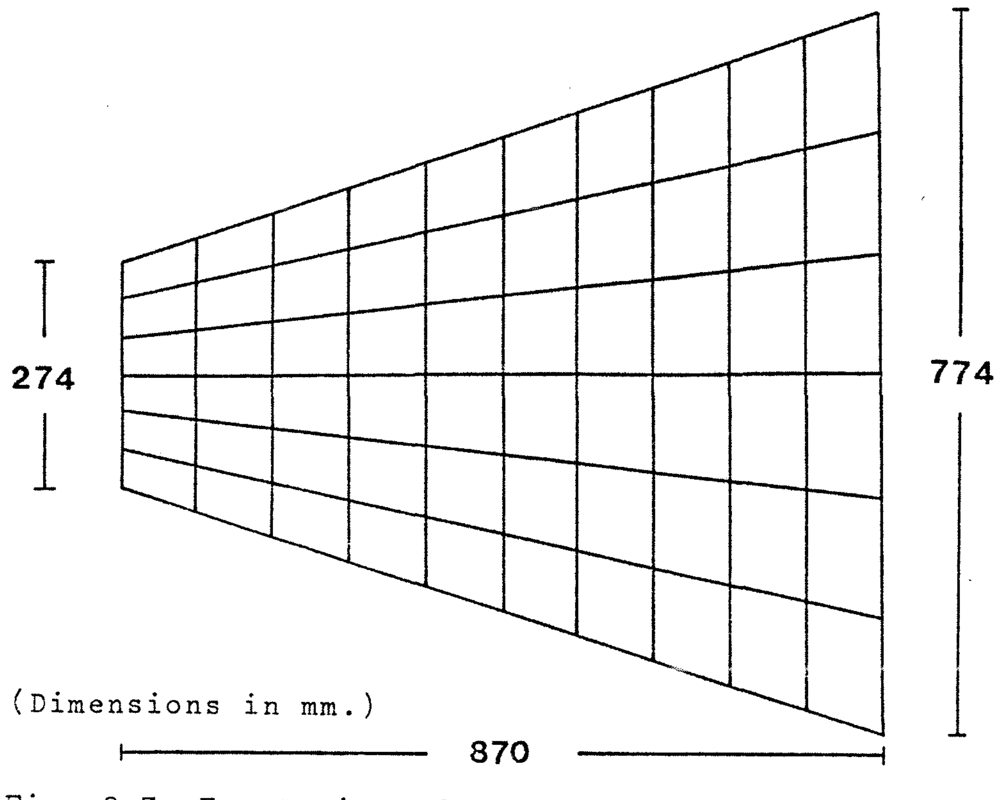

Fig. 2.7 Front view of one of the trigger hodoscopes showing 10 vertical and 6 wedge-shaped bars of scintillators.

d) compton scattering

The relative cross-sections of these processes are shown in fig. 3.1 and 3.2.

Process a) is responsible for the definition of the quantity "radiation length", X_o, which is a length characteristic for the material, through which an electron has to traverse in order to reduce its energy to 1/e of the original value, due to radiation only. It can be shown that the average energy loss due to radiation of an electron passing through matter is proportional to its instantaneous energy.

3.1.1 $$\frac{dE}{dx} = -\frac{1}{X_o} E$$ hence

3.1.2 $$E(x) = E_o e^{-\frac{x}{X_o}}$$

where E_o is the original energy of the electron, x is the distance in radiation lengths it has travelled in the material, E is the energy of the electron at a depth x.

Theoretical derivations of the value of X_o can be found in [16]. Qualitatively it is obvious that X_o decreases with increasing electron density, hence with the density of the material.

A rapid estimate of X_o, correct to within 20%, is given by:

3.1.3 $$X_o \approx 180 \frac{A}{Z^2} \text{ g/cm}^2$$

The most serious background in our experiment, is the production of π^os with its subsequent decays to $\gamma\gamma$ final states. The two gammas will often appear (in the lab. system) with a very small opening angle. This may cause the two γ showers to be interpreted as originating from one γ only. For this reason it was decided to optimize the calorimeter for position resolution and one versus two-shower discrimination. The calorimeter is thus in three parts, first a lead scintillator sandwich of thickness 4.7 X_o, then a set of four wire chambers with analog read-out of the cathode strips, and at last a lead glass wall of thickness 10 X_o. An electromagnetic shower at our energies has its maximum after about 4 - 5 X_o. The best position measurement of a shower is done at the shower maximum, and this is the reason for the choice of thickness of the first part of the calorimeter (the precalorimeter).

b) The precalorimeter.

The precalorimeter consists of a 1cm thick iron plate, 10 layers of segmented scintillation counters, each 0.5 cm thick, interspaced with 9 layers of lead, each 0,25 cm thick. This gives a total of 4.74 X_o of material. The scintillation counters consists of 5 layers of 14 nearly horizontal rods and 5 layers of 29 vertical rods. A set of 5 rods from the 5 layers is seen by one photomultiplier*, see figs 3.4 and 3.5.

The signal from a PM is split into two parts; one containing 9/10 of the original signal, the other contains 1/10 of the signal. The signals are time integrated in LRS** 2249A Analog to Digital Converters. The splitting of the signal increases the dynamic range of the precalorimeter by a factor ten.

*Phillips XP 2262 with Base CERN 4244

**LeCroy Research Systems.

of the blocks are 15x15x30.5 cm^3, which corresponds to 10 X_o of material. The blocks are arranged as shown in fig. 3.9, and each block is viewed from behind (from the target end) by an EMI* 9928KA photomultiplier, which has a cathode diameter of 12.5 cm.

3.3 Physics, preliminary tests and construction of the LG walls.

A. Physics in the Lead Glass and Phototmultipliers.

The electrically charged, energetic, shower particles in the Lead Glass are moving faster than the speed of light in this medium. Thus, Cerenkov light is emitted. Since the lead glass is transparent to visible light; part of the Cerenkov light is transmitted through the lead glass, and can be collected at a photocathode.

The number of photons per unit path length of a relativistic unit charge particle and per unit wavelength is given by [19]

3.3.1 $$\frac{d^2N}{ds\,d\lambda} = \frac{2\pi\alpha}{\lambda^2}\left(1-\frac{1}{n^2\beta^2}\right) = \frac{2\pi\alpha}{\lambda^2}\sin^2\theta$$

where $\alpha = \frac{e^2}{\hbar c}$

λ = wave length

n = refractive index of the medium (the lead glass)

β = the speed of the charged particle in units of c, the speed of light in vacuum.

θ = the angle of emission of the light, the Cerenkov angle.

Note the $1/\lambda^2$ dependence of the number of photons emitted. This makes high transmission of blue and U.V. light desireable. Of the lead glasses

*EMI Industrial Electronics Limited, Hayes, England.

The number of photoelectrons produced from a shower at our energies is such that this is the major source of fluctuations in the signal output. Since the fluctuations, σ, in the number of photoelectrons, N, is proprtional to $\sqrt{N}$, this will show up as a $E^{-\frac{1}{2}}$ dependence of the energy resolution of the counter. Appendix 1 gives a derivation of this, and of the fundamental properties of photomultipliers. It is thus essential for a good energy resolution of the counter to collect as much as possible of the Cerenkov light at the photocathode. The PMs were glued directly onto the lead glass, and the photocathode was chosen to be as big as possible compatible with the practical construction of the lead glass wall. The glue used is of the type Kodak HE 104-2:, and has a refractive index which lies between the refractive index of the lead glass (n=1.62) and the refractive index of the PM window ($n \approx 1.5$). This gives optimal transmission of the light from the lead glass to the photocatode. The photocathode has a diameter of 12.5 cm, while the cross section of the lead glass blocks is 15x15 cm^2. This gives a coverage of about 55% of the back area of the blocks; and the light collection effeciency is limited to 55% for this reason.

There are also fluctuations in the number of photons reaching photocathode due to fluctuations in the position of the initiation of the shower. Light initiated early in the lead glass will be attenuated more than light initiated later, before the cathode is reached. Moreover, this effect is biggest at short wavelengths, where transmission is lowest and the number of photons produced is high. In our calorimeter, a shower of particles produced in the very dense lead scintillator precalorimeter hits the lead glass

PMs must be shielded from electric and magnetic fields to minimize the noise. Background fields are always a problem in an eletronic experiment, because of all the high tensions around. We tested a block of SF5 lead glass of dimensions 14x14x47 cm^3 with one of our PMs glued to it. This was before we had purchased any lead glass. The wrapping of a lead glass block is shown in fig. 3.12, and the testblock was wrapped in a way which is equivalent electrically (but some of the materials were different). During the test, we did not have any noise problems, hence this way of wrapping was adopted.

The PM is shielded by a μ-metal magnetic shield [20] connected to the same potential as the cathode, negative HT. This shield is glued to the lead glass with conductiong araldite. The innermost layer of the wrapping is conducting aluminized mylar connected to the μ-metal shield. Thus the whole block should be at the cathode potential, and polarizarion effects in the lead glass are avoided. Such a polarization field would disturb the potentials in the PM. Outside the mylar is a layer of black light-proof and electrically insulating Polyvinylchloride (PVC). Outside the PVC is an electrostatic shielding, a metal foil called conetic foil [21], which is the same potential as the anode which is at ground. Finally there is a layer of insulating mylar [22]. Thus every block is insulated from eachother, so no electrical crosstalk is possible. E.g. if the black PVC of one block gets scratched, and the conetic foil gets a high tension, this will not affect the other blocks, (it is very unlikely that the PVC will be scratched).

ii) Lineraity and energy resolution.

The first tests were done with a prototype of the bases to be used in the experiment.

C. Some tests using a Light Emitting Diode (LED).

For these tests we used a green LED, HP 5082-4950 which has its dominant wavelength at 572 nm. On some occasions two LEDs were used. The charge, q, deposited at the PM anode was measured in a LRS 3001, where the signal current is integrated over a time interval defined by an external gate. (Optionally, the unit generates an internal, threshold triggered gate). The unit has a memory capable of storing the results of many integrations. The q(charge)-distribution of the integrations can immediately be displayed as a histogram on any oscilloscope; so no sophisticated read-out is necessary. The range of the unit is from zero to 256 pC in steps of 0.25 pC (i.e. 1024 channels) just like in the LRS 2249A ADC. The general logic for these tests is outlined in fig. 3.15. For a general review of the NIM standard logic units see ref.[24].

i) Test of PM stability.

The LED was connected to a lead glass block via an optical fibre, so that the PM recieved light pulses through the lead glass. The LED was pulsed continously for 14 days, and q-distributions were taken (almost) every day during this period with the LRS 3001.

Fig. 3.16 shows that the response from the PM varies conciderably. The signals have a variation of more than 15% showing that the PM's must be monitored carefully. However, we should have in mind that there is no monitoring of the LED's stability during the test.

ii) Test of signal attenuation in cables.

The signals from the lead glass will be transmitted through about 80 m of cable, in the experiment. The cable material is dispersive, (i.e. different frequencies of the Fourier decomposition of the pulse moves with different lead glass. We tested 129 of the 132 PMs (the rest were not available at the time of test) using a pulsed LED in a light proof cupboard. The distance between the LED and the PM could be altered and measured very accurately. When the PM was at its closest distance from LED, the light output of the LED was set to give a signal comparable to that from a shower generated by a 3-4 GeV electron in lead glass. The estimate of the light output was made using the data from the tests of a lead glass block in an electron beam (p 38÷39). The high tensions on the PMs were set so that this signal gave a nearly full scale response on the LRS 3001 qVt, i.e. $\bar{q} \sim$ 800-900 channels above the pedestal.

We did some crude measurements of linearity and voltage dependence of the signals.

a) Linearity

q-distributions were taken at 4 distances from the LED, 30, 60, 90 and 120 cm. In calculation of the flux falling onto the cathode; the LED can be treated as an isotropic point source; but the PM cathode diameter was too large to assume a perfect inverse square law of the integrated light flux. Instead we used this expression for the integrated flux ϕ

3.3.3 $$\phi(d) = \int_{\text{PMsurface}} \frac{K\mathbf{r}\cdot\mathbf{n}}{r^3}\, ds = K\left(1 - \frac{d}{\sqrt{d^2+r_o^2}}\right)$$

where d is the distance from the LED to the cathode centre,

r is a vector from the LED to a point on the cathode

r_o is the radius of the cathode. At d=30 cm this provided for a 4% correction

A small change in γ will produce a big change in $\bar{q}$. This is one of the reasons why a stable gain monitoring system is so important.

Data were taken at 4 high tensions, and fitted to a function of the form given above, with K and γ as free parameters. (To avoid excessively big and small numbers, the fit was actually done to the logarithm of the expression.) The values obtained for γ are histogrammed in fig. 3.21. The response of some tubes vs.voltage is shown in fig.3.22. The deviation of any measurements from the fits was less than 2% in 85% of the measurements.

There are however some sources of instabilities in these measurements. The most important one is that one did not have time to let the photocathodes stabilize after that they were exposed to light. To be able to test all the tubes, we had to start the measurements immediately after that the PM's were installed in the cupboard, and we had to open the cupboard each time we wanted to alter the distance between the LED and the PM. The LED was not monitored, but during the time it took to make the measurements for one PM, we can assume that the fluctuations in the LED output are small. The primitive readout system may also have caused misreadings of the $\bar{q}$-value.

It must be mentioned that measurements of the linearity of one tube have been done under very well controlled conditions by Kim Kirsebom at the University of Oslo. This tube was found to be very linear.

3.4 Monitoring of the lead glass wall

The main source of systematic fluctuations in the calorimeter response

The ideal monitor is a stable pulsed light source with the same intensity spectrum as the Cerenkov light. Minimum ionizing particles, ($\pi^{\pm}$ and $\mu^{\pm}$ which passes straight through the lead glass without initiating any kind of shower) is such a monitoring source. Although the counters responce to minimum ionizing particles will always be a useful quantity to know, it is impossible to base the monitoring on these particles because of triggering and rate difficulties.

Three independent systems have been developed for the monitoring of the lead glass. Two of these are electrically pulsed light sources; one consisting of several yellow LED s the other is an argon gas filled glow lamp. The third system are buttons of scintillators with a few nCi radioactive americium.

The light from the pulsed lamps is sent onto the blocks via optical plastic fibres which are connected to the blocks at the same side as the PM s The reason for this connection point is that there is not enough space between the analog chambers and the lead glass to have them connected at the opposite side of the PM s The connectors used are in three pieces and they are made by AMP inc.* Connection points and connectors are shown in fig.3.24. The bushing was originally intended for splicing fibres, so we had to cut and polish this part; which was glued onto the lead glass with cyanolit (cyanoacrylate). These connectors are cheap, but we had to test them for stability. Due to transport problems we had to undo the fibre connections after the calibration of one wall, and the light signal intensities should be reproducible, after reconnection, to within 1-2%. We tested the connectors using the schematic layout of fig.3.15, with two LED s one untouched to be used to monitor the PM; while the other sent flashes through a connector

*AMP inc. Harrisburg, Pa., USA.

This fits the Cerenkov spectrum better than the LED wavelength-spectrum. Effects due to yellowing should therefore be better monitored with this lamp. The problem with this lamp, however, is that it has a slow decrease in light yield with time. It also has a limited lifetime (expressed in number ~~and~~ of pulses). These effects have been carefully studied [31](in Rome). With a stable monitor of the lamp one should be able to extract effects due to yellowing of the lead glass, and cathode fluctiations. The gain can also be monitored with this lamp, but due to the short lifetime, one will leave the continous control of this to the LEDs.

In addition to these systems, Am^{241} (α-sources), embedded in a plastic scintillator material, NE-102, are glued onto each block. (See fig. 3.12). The α-particles of energies 5.44 and 5.49 MeV cause the scintillator to emit light which is then transmitted through the lead glass to the PM.

In order to produce a gate for these pulses, one has to trigger on the PM pulses themselves. This is done by taking the signals from the 11th. dynode of the PM (see fig.3.11). The multiplication process of electrons in the PM dynodes, leaves excessive positive charge in the dynodes. Positive pulses are therefore generated. On the 11th dynode the positive pulse is equal to the negative pulse on the anode. The triggering system is shown in fig.3.26. With this logic one is able to take spectra of all blocks at the same time, hence not very time consuming.
One pulse in one block causes integration of all counters. Hence, in 131 of the 132 counters, just the pedestal will be measured. The pulse height distribution of a counter, will be a huge peak for the pedestal, and hardly anything else. However the peak due to the americium signal is easily observed if one

the maximum number of entries. The pedestal value was found similarily, using 5 channels to compute the mean value.

The americium q-distributions were also fitted to gaussians. The two methods agreed on the mean value to within ½ channel in most cases. Some runs had poor statistics and this is the reason for disagreements between the methods.

The mean values were in most cases at around 20 ch above the pedestal. If one then assumes an uncertainty in the peak position of 0.5 channels, this gives a 2.5% error in the peak position. Fig.3.31 shows the $\bar{q}$ histogrammed for 128 blocks. Even though the signals are as low as about 20 ch above the pedestal, it should be possible to obtain a very good estimate of the mean value. If the statistical sample is large enough, we are certain that the mean value can be estimated to an accuracy of 1%.

CM-energies of 3.5 GeV is close to 5 GeV. (see appendix 2). Taking into account that the signals will fluctuate, we decided that the minimum ionizing particle should produce a signal of about 5-6% of the full ADC scale. This means that the minimum ionizing peak should be 110 channels above the pedestal. The beam used during the calibration contained mainly minimum ionizing particles (π^-, μ^-) and only a few percent electrons. Thus we could take spectra with minimum ionizing particles very quickly, and use these spectra to set the high voltages on the photomultipliers. Mounted on support, the minimum ionizing particles passed through the lead glass blocks at an angle. This can, however, be corrected for as we studied the response of one block with incident particles at different angles. Fig. 3.32 shows the dependence of the signal on the angle of incidence for one block.

Minimum ionizing particles were also used for the first calibration of the precalorimeter. The precalorimeter consists of bars of scintillators which have a length of up to 1m. The attenuation of a scintillation signal depends on where it is produced with respect of the PM. Minimum ionizing particles were used to find the light attenuation in the scintillators as function of impact point.

We proceeded to take data with electrons at 1. 2. 3 and 4 GeV. The calorimeters were more carefully scanned at 3 GeV than at the other energies. From these data, all calibration constants can be determined. In other words; we can find the best algorithm for reconstructing the energy, given the ADC information. The gains of the photomultipliers were continously monitored during the test, and all signals will be normalized to some initial gain condition. The normalized signal can be written as:

The method consists of plotting Σq_{LG_i} against Σq_{pre_i} for all events of a run (at a certain energy and impact point), and finding the best straight line through these points. This line determines K_1 and K_2.

The second method consists in determining one calibration constant per counter, i.e.

3.5.5 $$E = \sum_{i=1}^{n} K_i q_i$$

where the sum runs over all counters both in the precalorimeter and in the lead glass wall, having a signal above a certain threshold. The best K_i's are found by summing the pulse heights for all events in a rún, and minimizing the sum of the squared differences, i e. minimizing

3.5.6 $$S = \sum_{i=1}^{Nev.} \left(E - \sum_{i=1}^{n} K_i q_i\right)^2$$

by putting

3.5.7 $$\frac{\delta s}{\delta K_i} = 0, \ i=1,2, \ldots n$$

This gives n equations to determine the n unknown constants $K_1 \ldots\ldots, K_n$.

Both methods seem to work, and they give approximately the same energy resolution. However, work is still under way to refine the methods in order to improve the energy resolution. Effects to concider are:

i) Nonlinearities in pulse heights.

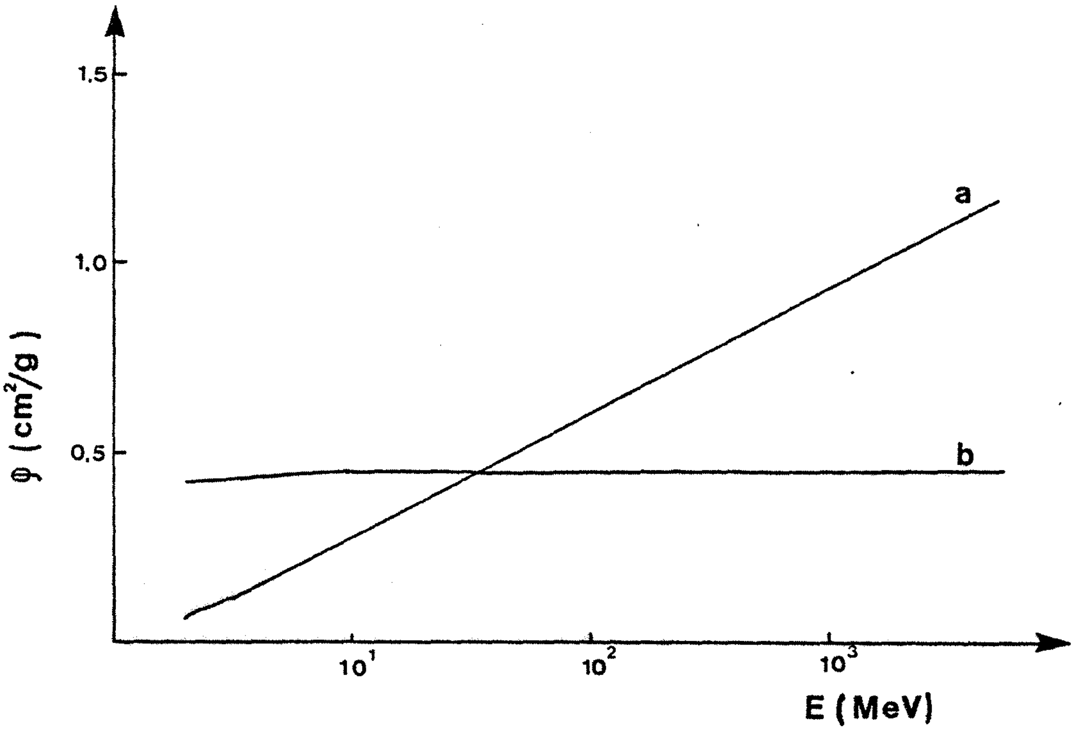

Fig 3.1 Rate of γ emission for an electron traversing 1 g/cm^2 of lead glass versus electron energy (a), and rate of electron-electron elastic collisions versus electron energy (b).

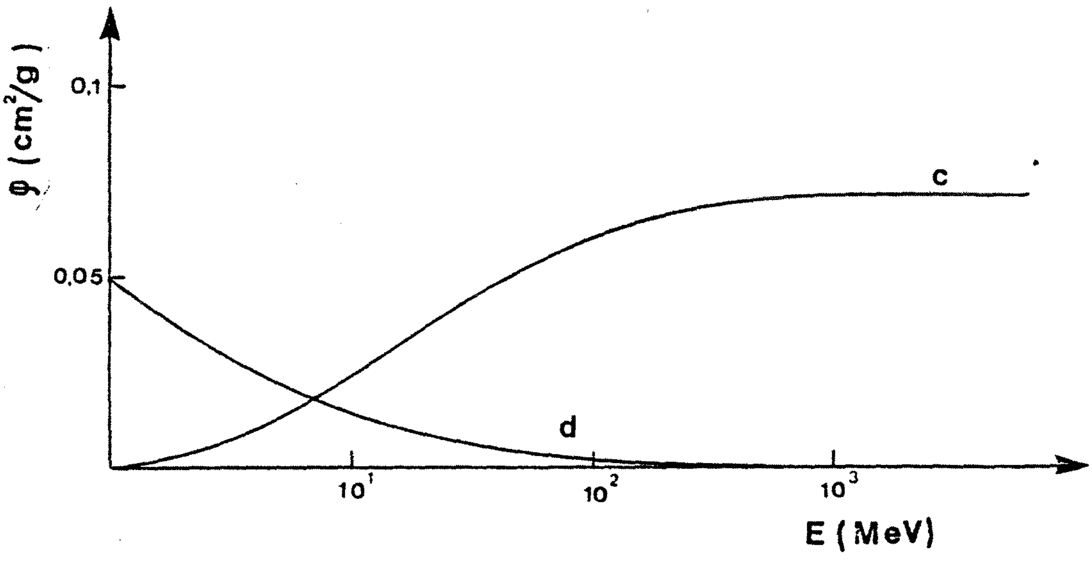

Fig 3.2 Electron-positron production rate for a photon traversing 1 g/cm^2 of lead glass versus photon energy (c), and rate of compton scattering versus photon energy (d).

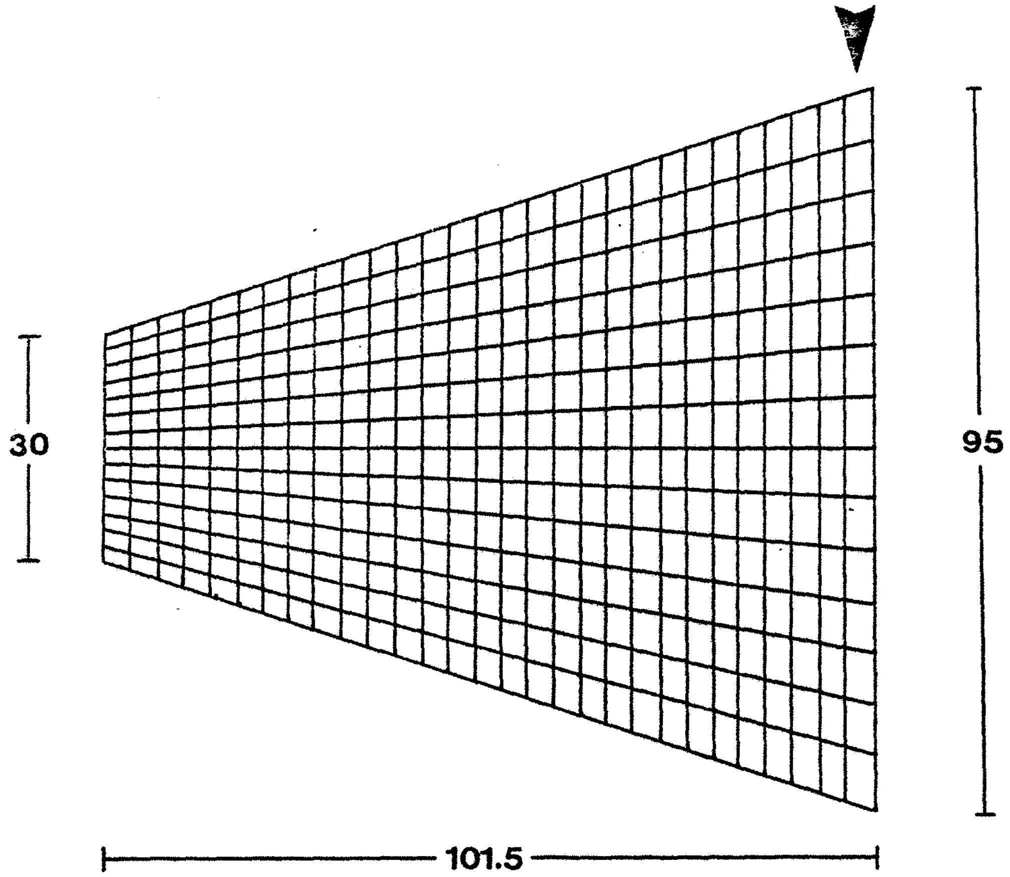

Fig. 3.4 Front view of one of the precalorimeter arms consisting of 29 θ-counters of width 3.5 cm,and 14 φ-counters which are wedge shaped with smallest width 2.1 cm, and largest width 6.8 cm. Dimensions in cm.

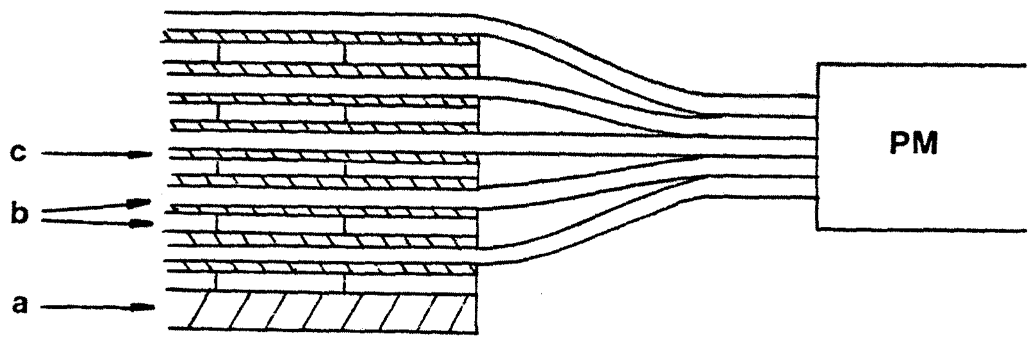

Fig. 3.5 Top view of the precalorimeter. The arrow in fig. 4 shows the viewpoint.
a= iron
b= scintillator
c= lead

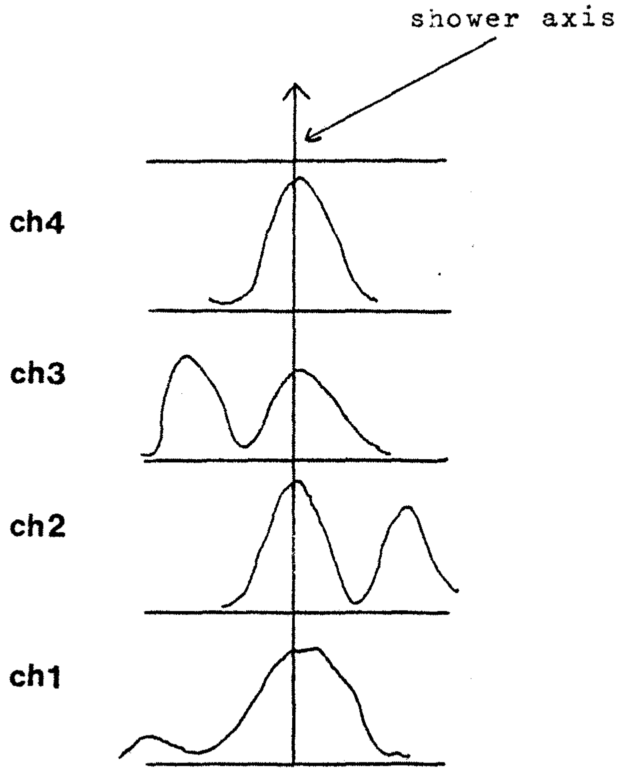

Fig. 3.8 illustrates the effect of highly ionizing slow particles. The pulse heights of fired strips are shown, and some of the peaks clearly don't correspond to the position of the shower axis.

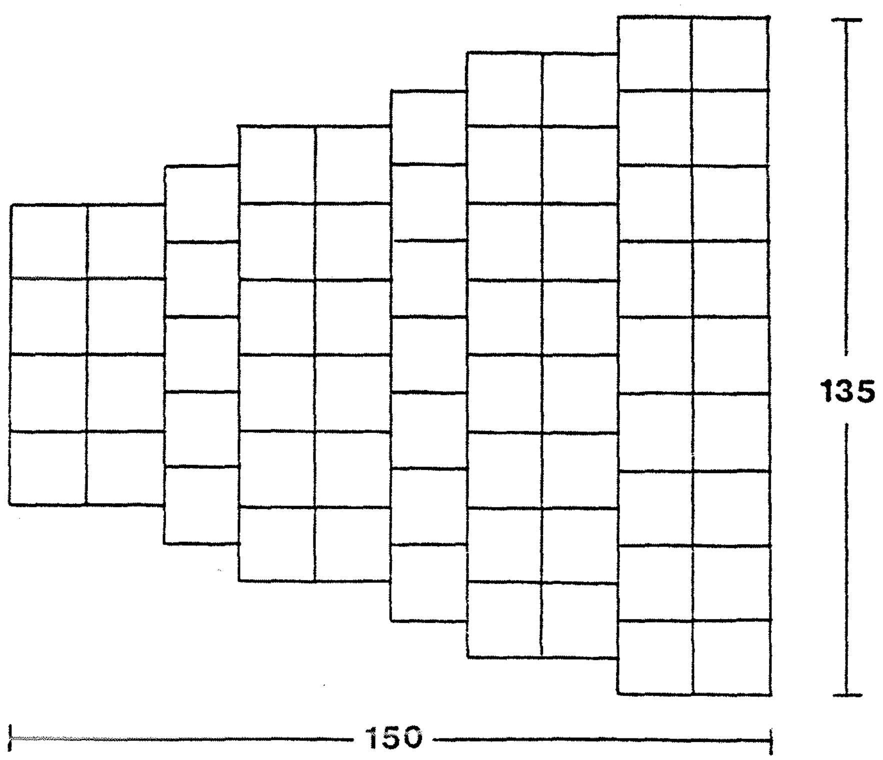

Fig. 3.9 Front view of one of the lead glass walls. Due to the thickness of the wrapping material, the dimensions (in cm) are slightly bigger than those indicated. The photomultipliers are mounted behind the wall.

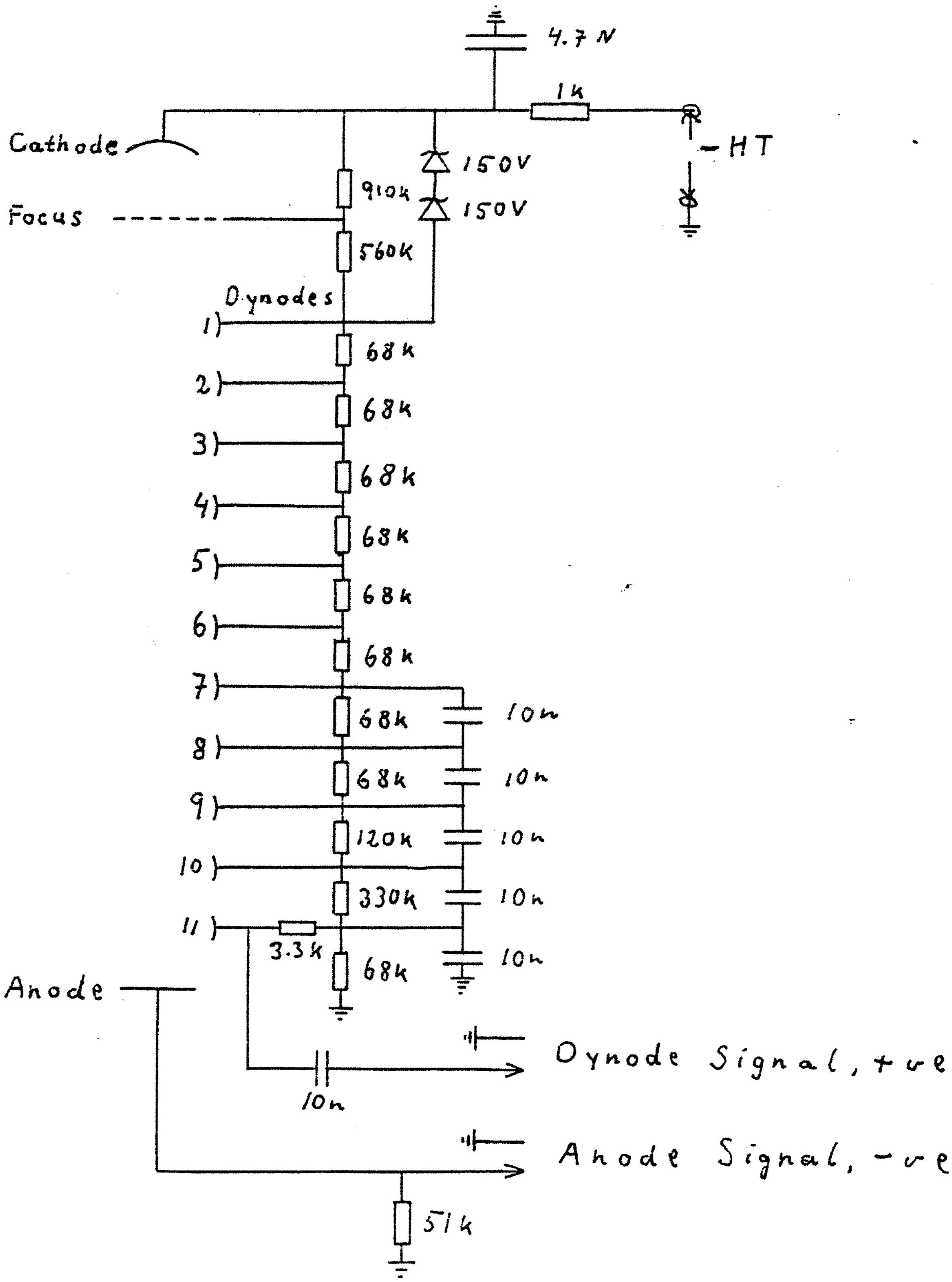

Fig. 3.11 Base design.

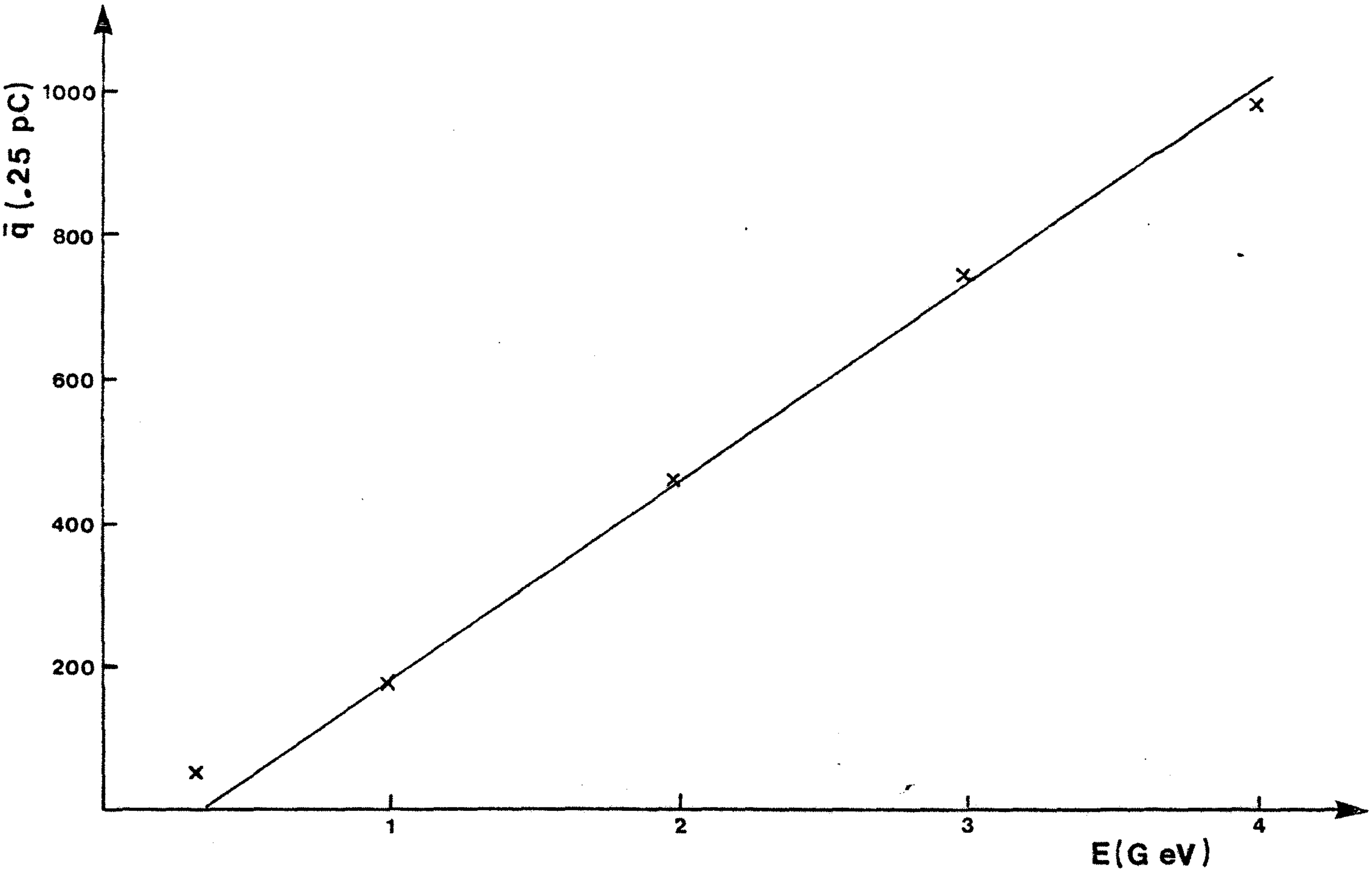

Fig. 3.13 Mean integrated charge versus beam energy

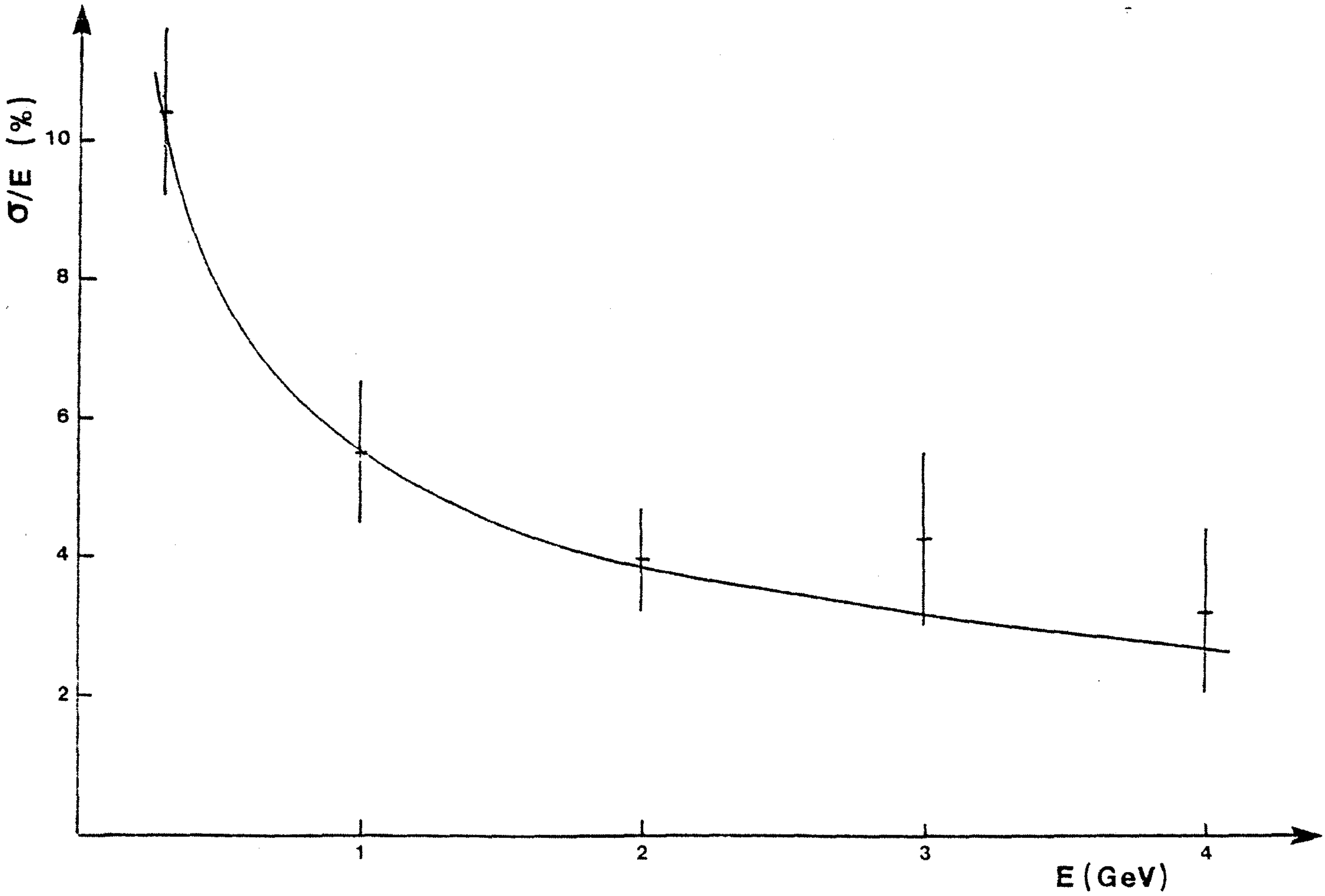

Fig. 3.14 Energy resolution versus energy. The curve is $F(E) = 5.5\%/\sqrt{E}$

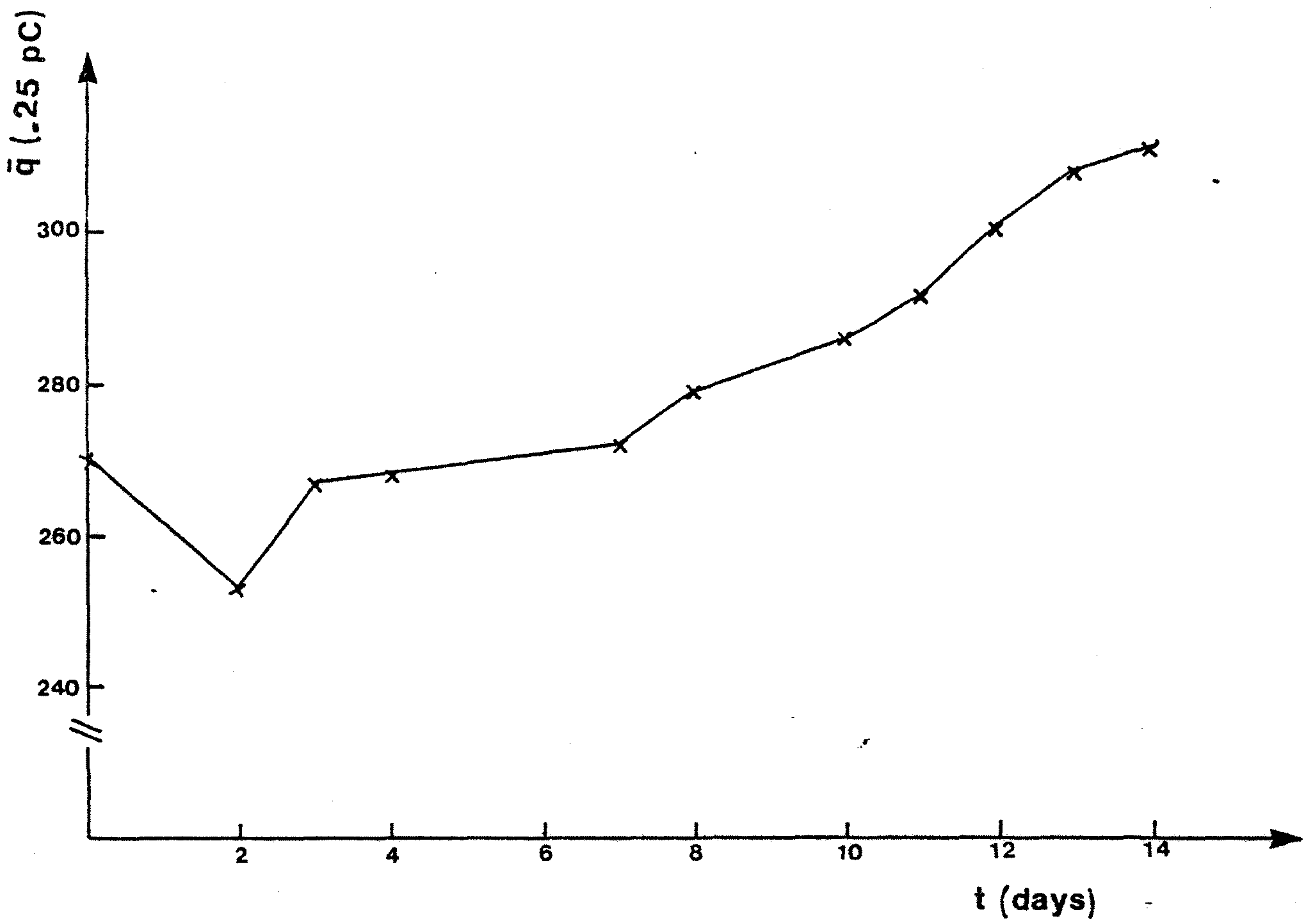

Fig. 3.16 Photomultiplier response over a period of 14 days.

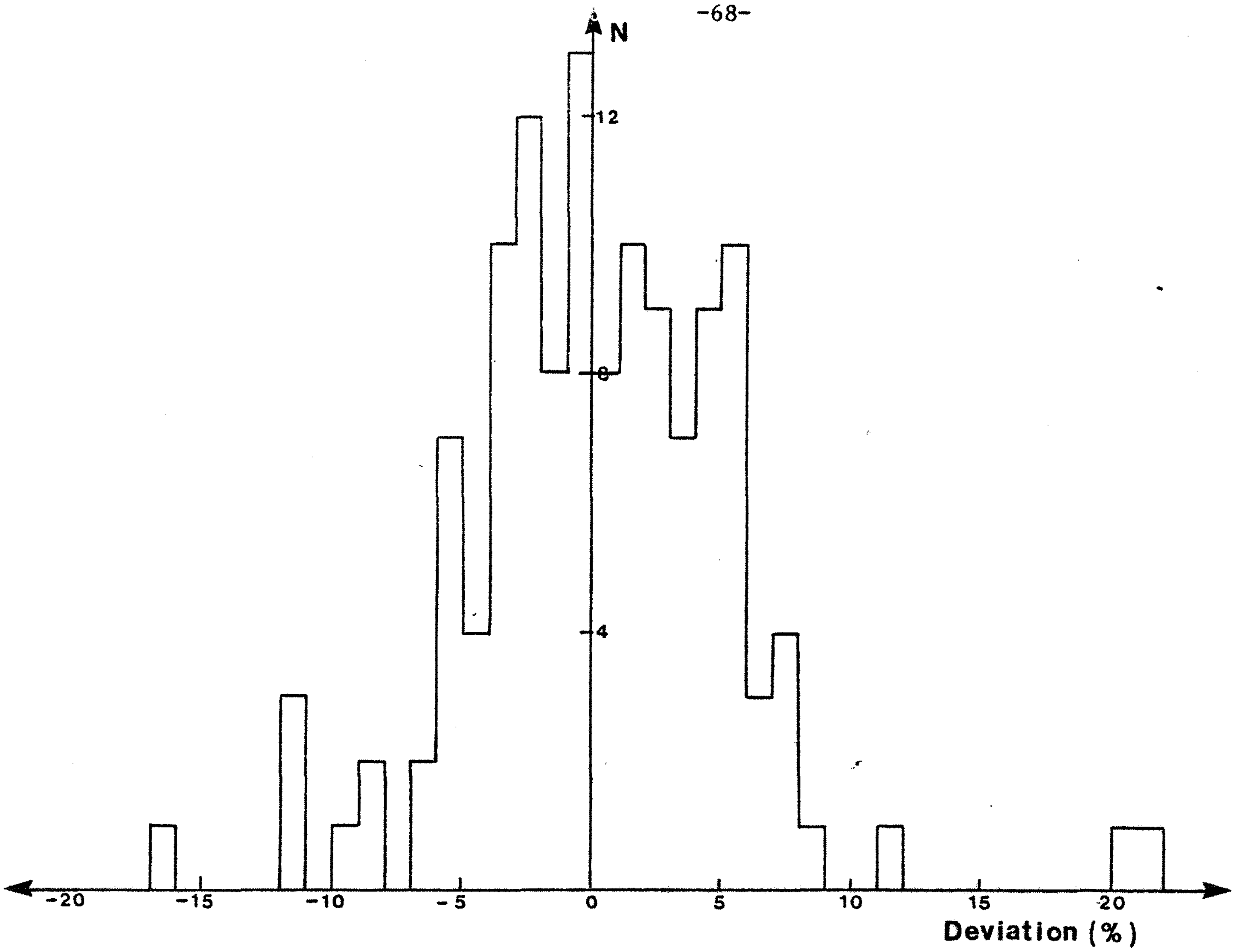

Fig 3.19 Deviation from linearity of the biggest signal for the tubes. Mean=0.3% , rms=5%.

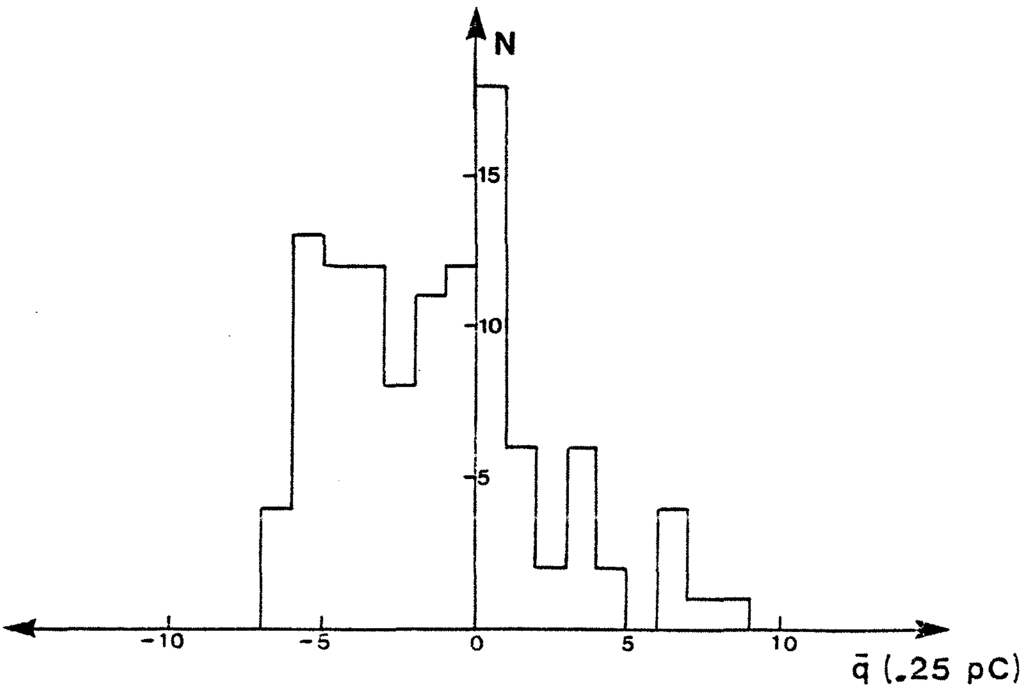

Fig 3.20 Extrapolated deviation from the origin in number of channels. Mean=-2ch. , rms=4.5ch.

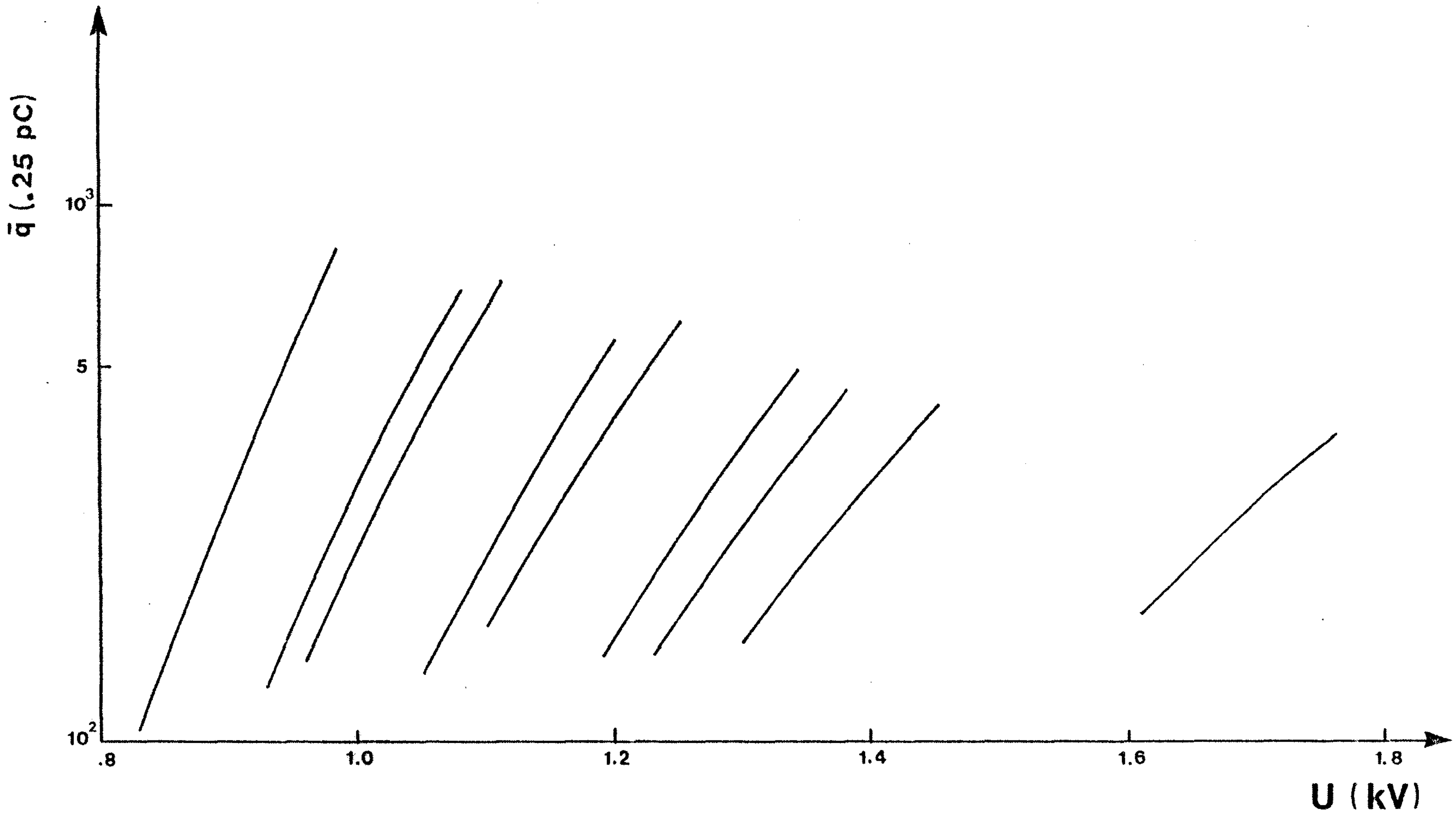

Fig. 3.22 Mean integrated charge versus high tension for some tubes. The LED signal is fixed.

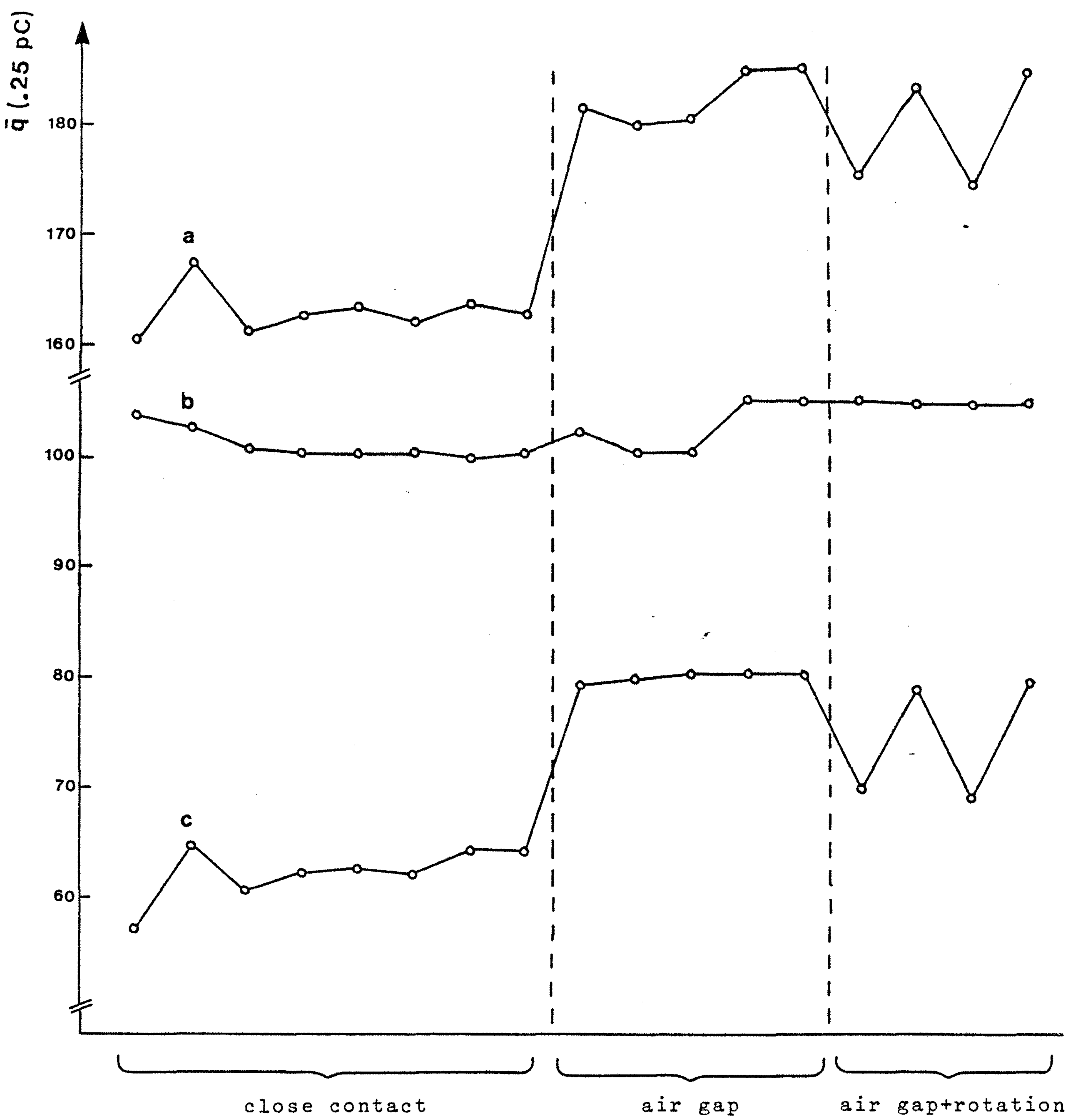

Fig. 3.25 Between each point, the fibre is disconnected and reconnected.

a = The mean value of the charge from the light passing through the connector to be tested.
b = The mean value of the charge from the undisturbed light source.
c = The difference between the two values.

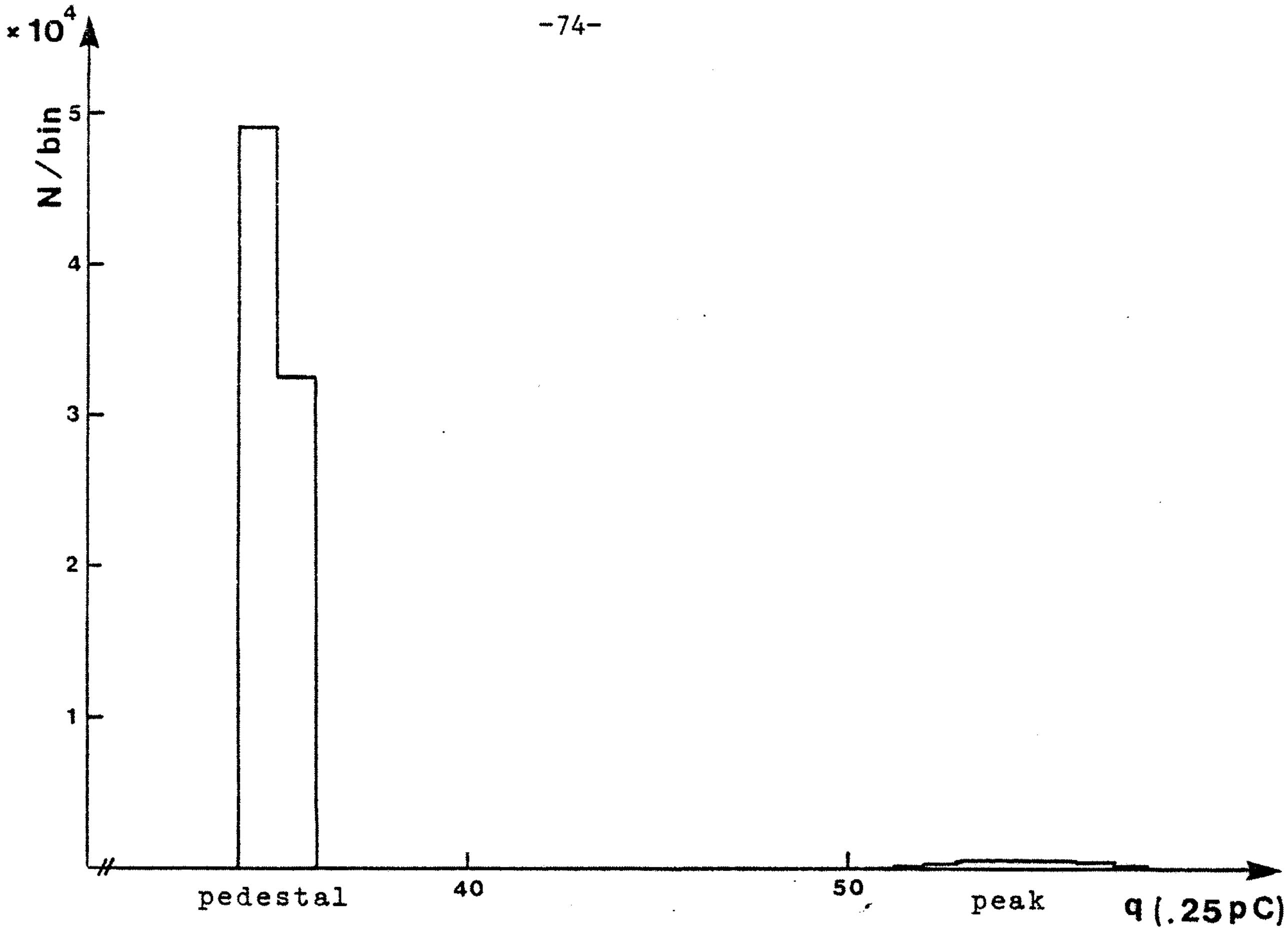

Fig. 3.27 All integrations in an ADC histogrammed. The pedestal is calculated from this to be p=34.4 ch. (using integer values of the channels,not the midpoint between two channels).

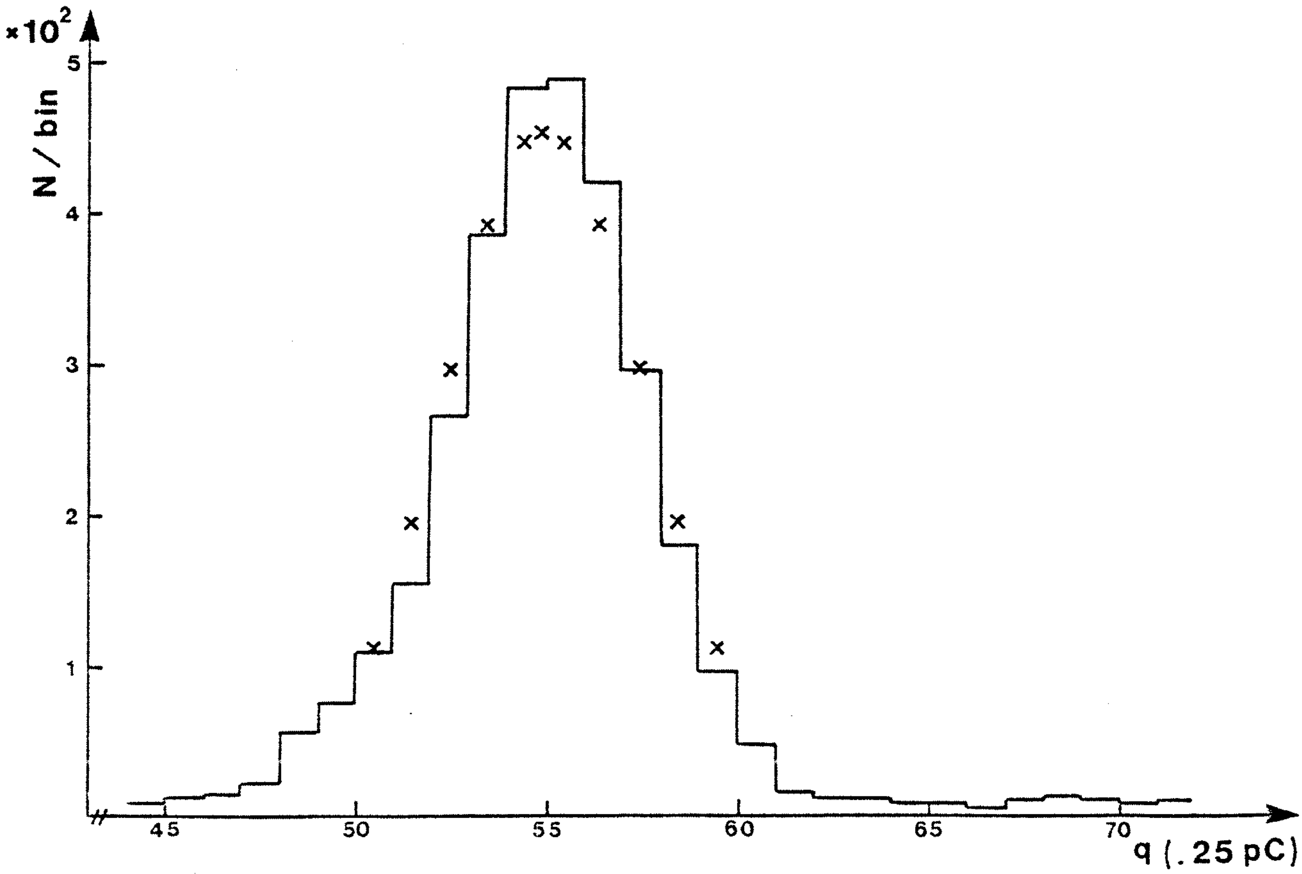

Fig. 3.28 The am-signal after suppression of the pedestal. Mean value $\bar{q}$=54.6 ch. $\bar{q}$-p=20.2 ch.
The crosses are function values of a gaussian fit giving $\bar{q}$-p=20.1 ch.

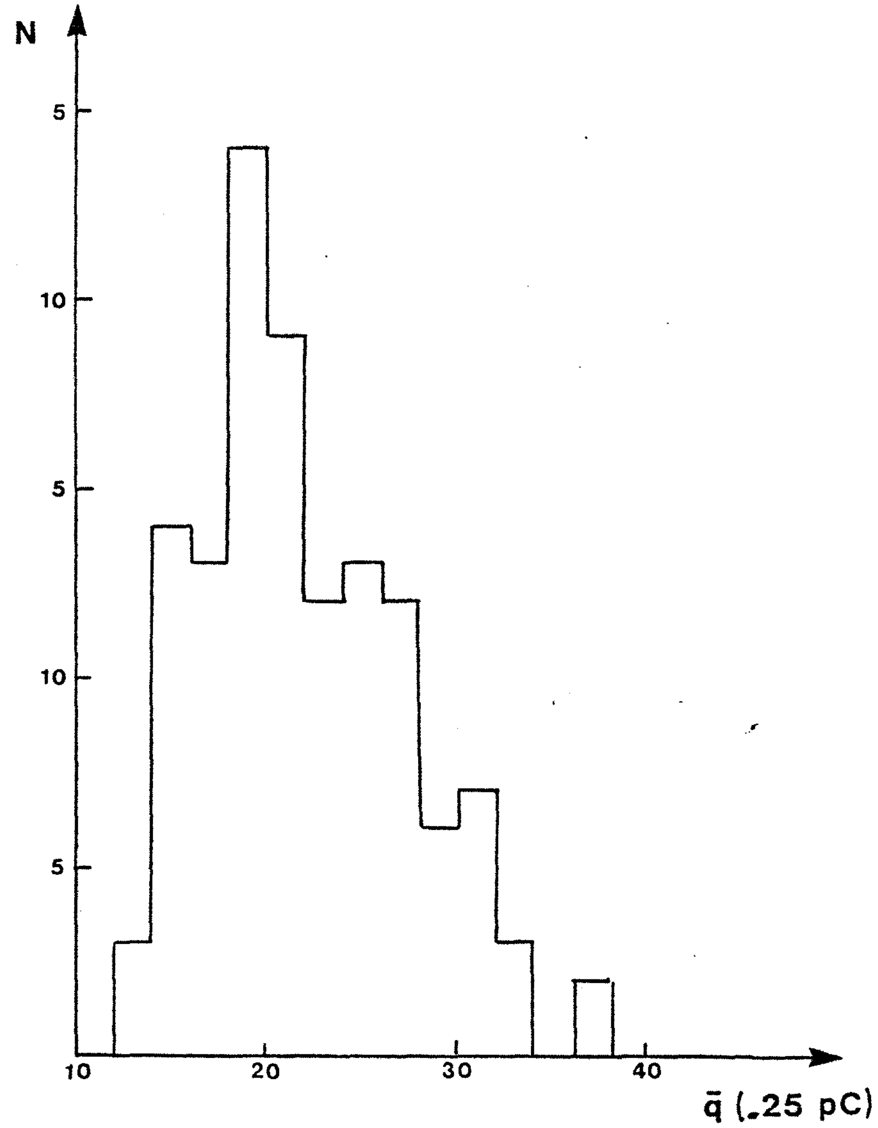

Fig. 3.31 Mean values of the americium signals for 128 of the blocks.

APPENDIX 1. CALCULATIONS CONCERNING PHOTOMULTIPLIERS.

If a fixed nonfluctuating number of photons of a certain frequency is falling onto the photocathode, the mean number of photoelectrons produced will be:

(1) $$\overline{N}_e = \varepsilon n_{ph}$$

where n_{ph} is the number of photons and ε is the probability for a photon to produce a photoelectron. The value of ε depends on the freqency of the photons and is always smaller than 0.25. ε is called the quantum efficiency.

A photo-electron can either be produced or not produced. Therefore the appropriate statitics to use is binomial statitics. This means that if one records the numbers, N_e , each time a stable pulse hits the cathode, these numbers will be binomially distributed with mean $\overline{N}_e$, and standard deviation given by:

(2) $$\sigma(N_e) = \sqrt{\overline{N}_e(1-\varepsilon)}$$

Since $\varepsilon<0.25$, $\sqrt{1-\varepsilon} > 0.85$. For yellow light $\varepsilon \approx 0.05$ and $\sqrt{1-\varepsilon} \approx 0.97$, so normally one can assume that $\sigma=\sqrt{\overline{N}_e}$, and poissonian statitics. In the following,however, the factor $\sqrt{1-\varepsilon}$ does not introduce complications.

The number of electrons are multiplied enormously throughout the dynode chain, and the charge deposited at the anode is given by:

(3) $$q = GN_e$$

where G is the gain of the photomultiplier. If we write q in units of the elementary charge, we have $G=N_a/N_e$ where N_a is the number of electrons at the anode. $G \approx 10^6$ in order of magnitude. The relative standard deviation of q from (3) is:

(4) $$\sigma(q)/\overline{q} = \{(\sigma(G)/G)^2 + (\sigma(N_e)/\overline{N}_e)^2\}^{\frac{1}{2}}$$

With our assumptions it is important to realize that (6) really is a lower limit for $\overline{N}_e$. Because of additional fluctuations it is more correct to write:

(5a) $$\sigma(q)/\overline{q} \geqq \sqrt{(1-\varepsilon)/\overline{N}_e}$$

instead of (5) ,so

(6a) $$\overline{N}_e \geqq (1-\varepsilon)(\overline{q}/\sigma(q))^2$$

Likewise it is more correct to write:

(7a) $$G \leqq (1/1-\varepsilon)(\sigma(q))^2/\overline{q}$$

instead of (7).

However during monitoring of photomultipliers, we are only interested in relative variations in the gain and in the number of photo-electrons produced, so the quantities $(\overline{q}/\sigma(q))$ and $(\sigma(q))^2/\overline{q}$ provide for a useful separation of effects, especially if we have instability-effects like yellowing of the lead glass or unstable monitoring light.

To derive the dependence of the signal on the overall voltage on the tube, one assumes that the gain, g_i, at each dynode is given by:

(12) $$g_i = kv_i^\alpha$$

where k and α are characteristic for the dynode material. The v_i s are the potential drops between dynodes d_{i-1} and d_i . There is usually a fixed focussing voltage between the cathode and the first dynode:

(12a) $$g_1 = kv_f^\alpha$$

APPENDIX 2. CALCULATION OF LABORATORY ENERGIES FOR A GIVEN CENTRE OF MASS ENERGY:

We want to determine the energy of the two decay products of charmonium as seen by the calorimeters.

In the laboratory system the situation is the following:

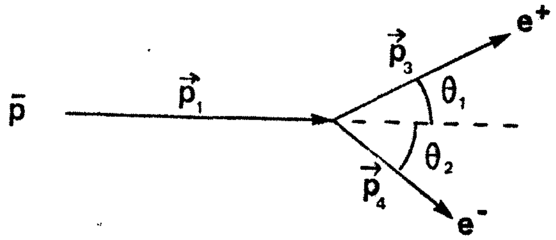

The incoming antiproton and the target proton are described by

$$q_1 = (\vec{p}_1, iE_1) \quad \text{and} \quad q_2 = (0, im_p)$$

In the centre of mass system the situation is:

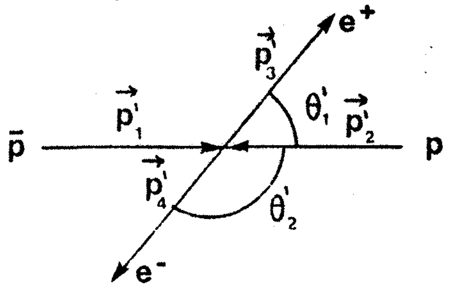

In this system, the four-momenta of the incoming particles are

$$q_1' = (\vec{p}_1{}', i\tfrac{1}{2}E^{cm}) \quad \text{and} \quad q_2' = (-\vec{p}_1{}', i\tfrac{1}{2}E^{cm})$$

Forming and equating invariants leads to:

(1) $$E_1 = ((E^{cm})^2 - 2m_p^2)/(2m_p)$$

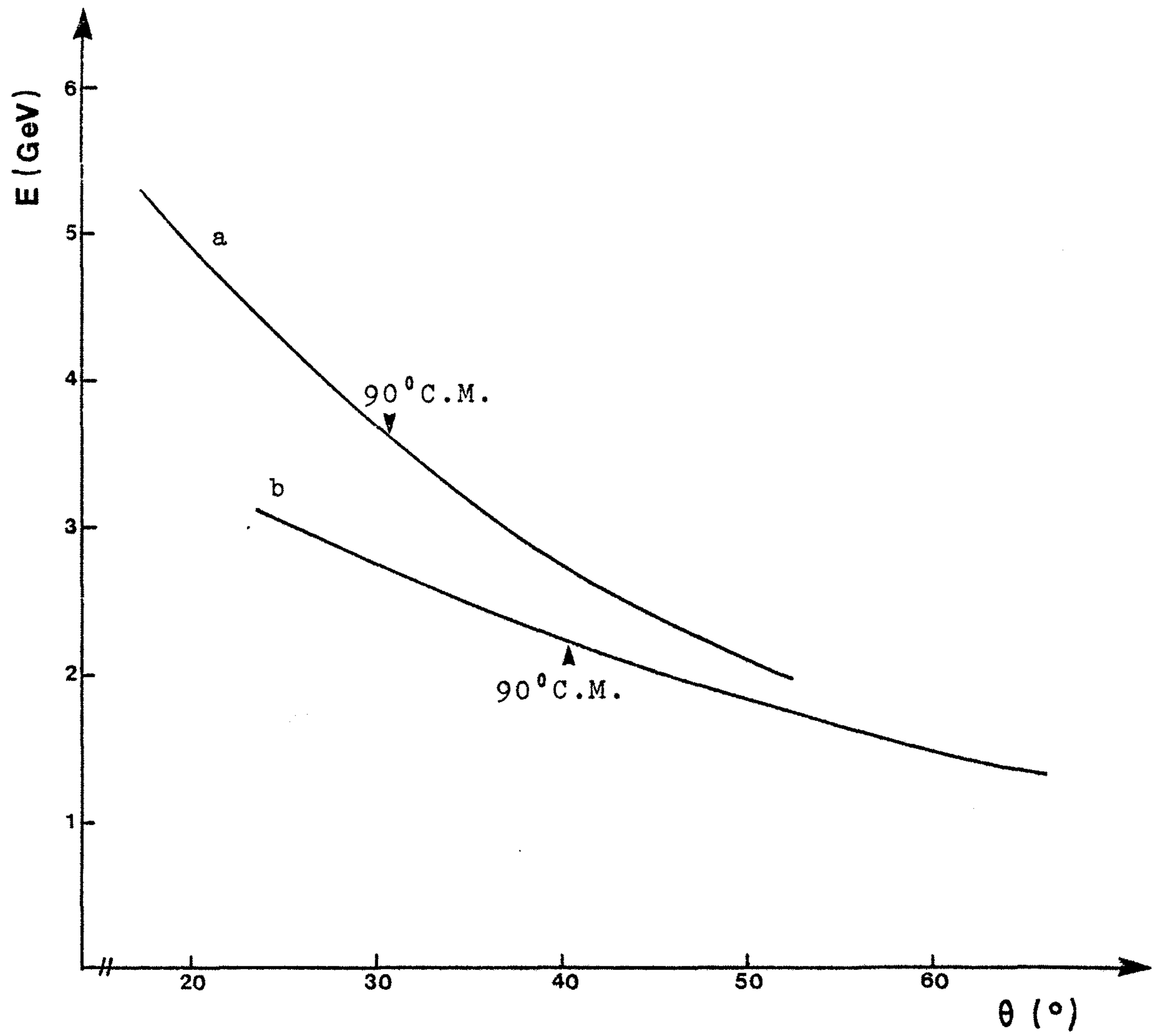

Fig. A2.1 Energy as function of decay angle in the laboratory frame at E_{CM}=3.7 GeV (a), and E_{CM}=2.9 GeV (b).

17. U. Amaldi, Physica Scripta 23(1981)409

18. Fig.3.3 is from E. Longo and I. Sestili, NIM 128(1975)283

19. J. V. Jelley, "Cerenkov Radiation and its applications", Pergamon Press 1958.

20. From Mecagis corp. France

21. From Denimex corp. N.Y. USA

22. Commercial name for Ethyl polyteraphtelate

23. A. E. Baumbaugh et al., NIM 197(1982)297

24. Kim Kirsebom. Thesis submitted to the degree "cand. real", University of Oslo 1981.

25. M. Goldberg et al., NIM 108(1973)119

26. Y.Yoshimura et al., NIM 126(1975)541

27. M. Holder et al., NIM 108(1973)541

28. F. Dydak et al., NIM 137(1976)427

29. Internal R-704 Report 29 by E. Menichetti

30. From "Review of Particle Properties", Phys. lett. 111B(1982)

31. M. DeVincenzi, F. Liello, M. Serveri, Nota Intarna n. 727, Istituto di Fisica G. Marconi, University of Rome.